Journal Name

ARTICLE TYPE

Cite this: DOI: 10.1039/xxxxxxxxxx

Efficient Hole Transfer from Monolayer WS_2 to Ultra-thin Amorphous Black Phosphorus†

Matthew Z. Bellus,[a] Zhibin Yang,[b] Peymon Zereshki,[a] Jianhua Hao,[b] Shu Ping Lau,[b] and Hui Zhao*[a]

Received Date
Accepted Date

DOI: 10.1039/xxxxxxxxxx

www.rsc.org/journalname

The newly developed van der Waals materials allow fabrication of multilayer heterostructures. Early efforts have mostly focused on heterostructures formed by similar materials. More recently, however, attempts have been made to expand the types of materials, such as topological insulators and organic semiconductors. Here we introduce an amorphous semiconductor to the material library for constructing van der Waals heterostructures. Samples composed of 2-nm amorphous black phosphorus synthesized by pulsed laser deposition and monolayer WS_2 obtained by mechanical exfoliation were fabricated by dry transfer. Photoluminescence measurements revealed that photocarriers excited in WS_2 of the heterostructure transfer to amorphous black phosphorus, in the form of either energy or charge transfer, on a time scale shorter than the exciton lifetime in WS_2. Transient absorption measurements further indicate that holes can efficiently transfer from WS_2 to amorphous black phosphorus. However, interlayer electron transfer of either direction was found to be absent. The lack of electron transfer from amorphous black phosphorus to WS_2 is attributed to the localized electronic states in the amorphous semiconductor. Furthermore, we show that a bilayer hexagonal BN can effectively change the hole transfer process.

1 Introduction

Recently, two-dimensional (2D) materials have drawn considerable attention for both fundamental research and applications due to their novel electronic and optical properties[1–5]. One of the intriguing aspects of these materials is that they can form multilayer heterostructures *via* van der Waals interlayer interaction[6]. Unlike ionic and covalence bonds, van der Waals interaction does not have atomic-level correspondence. This is a significant advantage over traditional heterostructures that can only be formed by materials with similar lattice structures. Since lattice mismatch is no longer a constraint, a large number of materials can be chosen from to assemble multilayers with certain properties. Hence, this new approach can produce a vast number of new materials for many applications, and can potentially transform material discovery[7,8]. The interfaces in such structures are atomically sharp and the junctions can be as thin as two atomic layers - both reaching the ultimate limit.

Since 2013, the study of van der Waals heterostructures has gained significant momentum. The majority of the efforts have been devoted to heterobilayers formed by transition metal dichalcogenides (TMDs) and graphene or by two types of TMDs, respectively. Combining graphene with TMD is beneficial for optoelectronic applications[9–12], since the former can serve as electrodes[13] while the latter, the light absorption or emission layer[14]. Study of TMD-TMD heterobilayers can provide valuable information on van der Waals interlayer coupling, and achieve tuning of the optical and transport properties of these materials[15–24]. In these van der Waals heterostructures, the two materials have similar lattice structures. Layer-coupled states can form, which can help integrate electronic and optical properties of the two materials. For example, layer-coupled states could be responsible for the observed ultrafast interlayer charge transfer in TMD-TMD heterobilayers[25].

The removal of lattice-matching requirements invites inclusion of materials with different lattice properties to form heterostructures. In principle, combining 2D materials with difference lattice structures (and thus likely different properties) can produce heterostructures with widely tunable properties. Demonstration of high-performance van der Waals heterostructures of materials with significantly different lattices structures will expand the material library and vastly increase the possible material combinations. Very recently, a number of 2D materials with different lattice structures have been used to successfully form heterostructures with TMD and graphene, including phos-

[a] *Department of Physics and Astronomy, The University of Kansas, Lawrence, Kansas 66045, USA. E-mail: huizhao@ku.edu*

[b] *Department of Applied Physics, The Hong Kong Polytechnic University, Hung Hom Kowloon, Hong Kong, People's Republic of China*

† Electronic Supplementary Information (ESI) available: Additional data on power dependence of the measurements. See DOI: 10.1039/b000000x/

phorene[26–29], GaTe[30], Bi_2Se_2[31], CrI_3[32], and even organic materials[33–37].

Here we introduce a noncrystalline semiconductor, namely amorphous black phosphorus (aBP), to the 2D heterostruture library. Amorphous semiconductors are of great importance in the electronics industry. They are an interesting class of materials, as their amorphous structure omits one of the most fundamental characteristics utilized in solid state physics, crystallinity. The lack of long-range periodicity often leads to very fuzzy electronic states and poor electronic performance compared to their crystalline counterparts. However, low fabrication costs make this type of materials highly desirable for applications that do not require superior performance. Most notably, amorphous silicon has been widely used for common photovoltaic devices[38] and thin-film transistors[39]. Amorphous In-Ga-Zn-O has shown promise for transparent thin-film transistors with reported mobilities exceeding 10 $cm^2\ V^{-1}\ s^{-1}$ [40]. Additionally, amorphous SiO_2 is widely used as a gate dielectric in the electronics industry. Amorphous materials have also been used as reaction catalysts, with amorphous iron being used to aid in the hydrogenation of carbon monoxide[41], and amorphous metal-oxides as an oxygen evolution reaction catalyst[42].

In this work, we fabricate heterostructures of monolayer WS_2 and 2-nm aBP, and study their charge carrier dynamics. Recently, ultrathin films of aBP have been successfully synthesized by some of us, along with other collaborators[43]. We found that in WS_2/aBP heterostructures, holes excited in WS_2 transfer to aBP on an ultrafast time scale. Electrons, on the other hand, do not transfer, neither from WS_2 to aBP nor the opposite direction. The charge transfer results in extended lifetime of photoexcited electrons in WS_2. We also show that a bilayer hexagonal BN (hBN) can slow down the hole transfer. These results introduce amorphous semiconductors to the library of building blocks for van der Waals heterostructures, provide a new ingredient for understanding the mechanisms of interlayer charge transfer, and offer a method to make electrical connections to amorphous materials through other 2D crystalline materials.

2 Experimental

2.1 Sample Fabrication

Amorphous black phosphorus ultrathin films were synthesized on Si/SiO_2 by pulsed laser deposition. A BP crystal was used as the target. The growth temperature was set at 150°C and the base pressure of the chamber was evacuated to 1.5×10^{-7} Torr. The nominal thickness of the film is 2 nm, according to previously established synthesis conditions[43].

The heterostructure samples were made by mechanically exfoliating and subsequently transferring monolayer flakes of WS_2 onto the aBP-covered substrate. In order to create reasonable control conditions, we first transferred flakes of hBN with varying thicknesses onto regions of the aBP substrates. This is done by mechanically exfoliating flakes of hBN from bulk crystals onto PDMS substrates. The hBN flakes are then transferred onto the aBP-covered substrate. Next, monolayer WS_2 flakes were similarly exfoliated onto PDMS substrates and identified by optical contrast. Using the same method as with hBN, they were transferred to the aBP sample, with different regions of the same WS_2 flake overlapping both the hBN layers and the aBP substrate. After the WS_2 was transferred, the samples were annealed for 2 hrs at 75°C in an Ar environment held at a base pressure of 3 torr. This is to help the van der Waals materials adhere better to the aBP. Next, to help preserve the aBP surface from degrading in the ambient conditions of our measurements, the samples were spin coated by a thin layer of PMMA.

2.2 Photoluminescence Spectroscopy

The PL spectroscopy measurements were carried out under a 405-nm continuous-wave laser excitation. The laser beam was focused by a microscope objective lens at normal incident. The laser spot is about 1 μm in full width at half maximum, and is located at the central part of a desired sample region. The power of the laser was controlled by a combination of a half-wave plate and a polarizer. The PL from the sample was collected by the same objective lens and directed into a spectrometer, which is equipped with a thermoelectrically cooled charge-coupled-device camera. To prevent the unwanted light from reaching the spectrometer and affecting the measurement, a set of filters was placed before the spectrometer.

2.3 Transient Absorption Measurements

In the transient absorption setup, a Ti:sapphire laser generates 100-fs pulses with a central wavelength tunable from 750 to 850 nm and a repetition rate of 80 MHz. Part of this beam was used to pump an optical parametric oscillator, which outputs a signal pulse tunable from 1100 to 1580 nm. The spectral range can be further extended by second harmonic generation of each output by using a beta barium borate crystal. Depending on the configuration, two of these pulses were used as pump and probe pulses.

In each configuration, the pump and probe beams were linearly polarized along perpendicular directions. A beamsplitter was used to combine the two beams, which were sent to a microscope objective lens and focused to the sample to spot sizes of 1 - 2 μm in full-width at half-maximum. The reflected probe was collected and collimated by the same objective lens and directed into a biased silicon photodiode, the output of which was measured by a lock-in amplifier that is synchronized with a mechanical chopper that modulates the pump intensity at about 2 KHz. We measured the differential reflection, which is defined as $\Delta R/R_0 = (R - R_0)/R_0$, where R and R_0 are the reflectivities of the probe by the sample with and without the presence of the pump beam, respectively.

3 Results and discussion

3.1 Sample and Photoluminescence

Figure 1(a) shows an optical microscope image of the sample studied. A uniform 2-nm aBP layer was deposited on a Si/SiO_2 substrate (see Methods), as shown as the pinkish colored background. To study effects of potential charge transfer between WS_2 and aBP, we first transferred a thick hBN flake on aBP (outlined by the white line). It contains more than 15 layers. We then

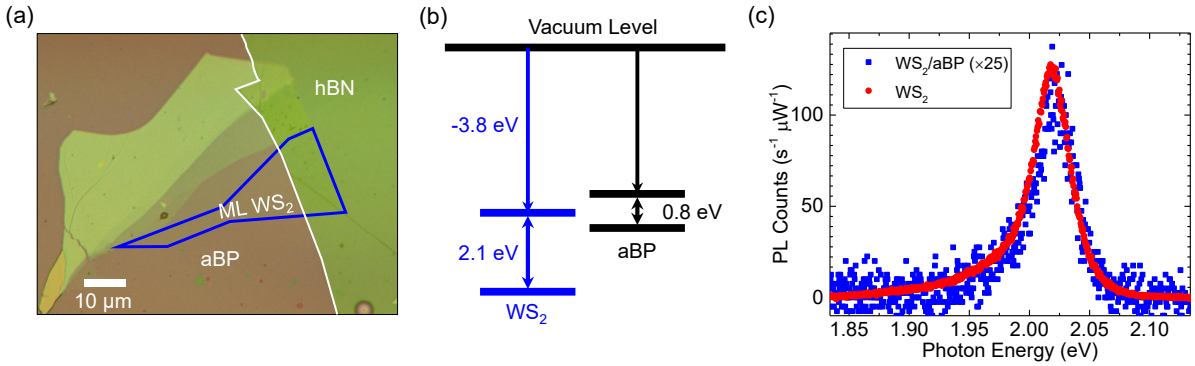

Fig. 1 (a) Optical microscope images of the WS_2/aBP sample. ML WS_2 is outlined by blue and hBN by white. Part of WS_2 is directly on top of aBP, while the rest is on hBN flake. (b) The expected band alignment of ML WS_2 and aBP. (c) Photoluminescence spectra of ML WS_2 directly on aBP (blue squares, multiplied by 25) and on hBN (referred to as WS_2, red circles).

transferred a monolayer (ML) WS_2 (outlined by blue) near the edge of the hBN flake. The region directly on aBP forms the heterostructure sample, while that on hBN serve as an isolated WS_2 ML for comparison, since the thick hBN layer is expected to block the interactions between WS_2 and aBP effectively.

From first-principle calculations, the electron affinity and the ionization potential of ML WS_2 are -3.8 and -5.9 eV, respectively[44], as schematically shown in Figure 1(b). Based on previous measurements, the optical bandgap of 2-nm aBP is about 0.8 eV[43]. However, information on the electron affinity and ionization potential of aBP is still missing. To speculate the nature of the band alignment of the WS_2-aBP heterostructure, one could use the values of crystalline BP as a reference. The bandstructure of crystalline BP is highly sensitive to thickness. Hence, one should use the values that best represent the 2-nm thick aBP, which correlates to about 3 layers. The calculated electron affinity of trilayer BP is about -4 eV[45]. Using the 2-nm bandgap of aBP of 0.8 eV, an ionization potential of -4.8 eV could be inferred. Given that this value is more than 1 eV from that of WS_2, it appears safe to assume that the valence band maximum (VBM) of aBP is above WS_2. However, since the electron affinities of the two materials are similar, the band alignment of WS_2/aBP could be either type-II, as indicated in Figure 1(b), or type-I with the conduction band minimum (CBM) of aBP below that of WS_2. In the following discussions, we will present evidence that the alignment is indeed type-II.

The sample was characterized by using photoluminescence (PL) spectroscopy. A continuous-wave 405-nm laser was focused through a 100× objective lens on to the sample. When the laser spot was placed on the WS_2 region on hBN, a strong PL peak at about 2.02 eV was observed (red circles). The PL yield, peak energy, and the lineshape are all consistent with previous reports[46–49]. This confirms the ML thickness of the WS_2 and the effectiveness of the thick hBN layer of separating WS_2 and aBP. In the rest of these discussions, we will refer this region of the sample as ML WS_2. With the laser spot moved to the region of WS_2 that is directly on top of aBP, there is significant quenching of the PL, by about a factor of 25 (blue squares). This quenching indicates that charge or energy transfer occurred from WS_2 to aBP. Without such transfer, excitons would be expected to stay in WS_2 and recombine, contributing to the PL signal. The large quenching factor suggests that such transfer occurs on a time scale that is much shorter than the exciton lifetime in an individual WS_2 ML.

3.2 Ultrafast Hole Transfer from WS_2 to aBP

The PL quenching of WS_2 by aBP can originate from charge transfer or energy transfer from WS_2 to aBP. In the former case, one type of carriers (likely the holes) transfer to aBP. Although the excited electrons reside in WS_2, they are separated from the electrons and hence cannot recombine with the holes and contribute to PL. In energy transfer, both electrons and holes transfer to aBP, which also results in a reduction of WS_2 PL yield. To resolve the transfer dynamics and probe the physics mechanisms involved, we performed transient absorption measurement in reflection geometry.

First, we studied photocarrier dynamics in the ML WS_2 region. Carriers are injected by a 3.2-eV pump pulse with a peak fluence of 0.46 μJ cm^{-2}. With an absorption coefficient of 0.72 $\times$ 10^6 m^{-1} [14], this corresponds to an injected areal carrier density of 4.37×10^{10} cm^{-2}. The red circles in Figure 2(a) show the differential reflection signal of a 2.0-eV probe, which is tuned to the A-exciton resonance of ML WS_2. The rise of the signal can be fit by the integral of a Gaussian function with a full width at half maximum of 0.37 ps, as indicated by the solid curve in the inset. Since the width of the pump and probe pulses are both about 0.25 ps at the sample location (due to the chirp introduced by the objective lens), this value is close to the instrumental response time. This suggests that the pump-injected electron-hole pairs produce a peak differential reflection signal at the A-exciton resonance on a time scale shorter than the instrumental response time, which is consistent with previous reports[50–52]. The decay of the signal can be fit by an bi-exponential function, $\Delta R/R_0(t) = A_1\exp(-t/\tau_1) + A_2\exp(-t/\tau_2) + B$. The black curve over the symbols show that the fit is satisfactory, with parameters of $A_1 = 1.51 \times 10^{-3}$, $A_2 = 1.19 \times 10^{-3}$, $B = 0.08 \times 10^{-3}$, $\tau_1 = 0.59 \pm 0.1$ ps, and $\tau_2 = 13 \pm 1$ ps. The bi-exponential dynam-

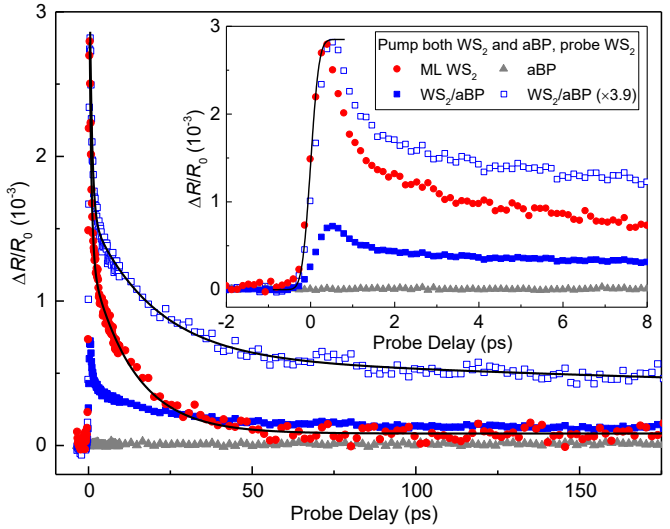

Fig. 2 Time-resolved differential reflection measurements with a 3.2-eV pump and a 2.0-eV probe. Solid symbols represent results from different regions of the same sample. Open symbols are scaled for better comparison. The inset provides a closer look of the data near zero probe delay.

ics and these time constants are both reasonably consistent with previous reports on ML WS_2 [50–52]. The short time constant of τ_1 can be attributed to formation of excitons from the injected electron-hole pairs [50]; while the long time constant τ_2 indicates the lifetime of excitons [51,52]. By increasing the pump fluence, we confirm that these time constants are independent of the injected carrier density, while the signal magnitude is proportional to the density (see ESI, Figure S1). To probe the possible contributions from the aBP layer underneath hBN to the signal, we repeated the measurement with the laser spots located at a region not covered by WS_2. The results are shown by the gray triangles in Figure 2. The lack of a detectable signal is expected [53], since the probe photon energy is much higher than the bandgap of 0.8 eV of the aBP layer.

We next repeated the measurement by moving the laser spots to the region of WS_2/aBP. Without interlayer transfer, one would expect a similar signal since the same density of carriers was injected in WS_2 and will produce a signal with the same time evolution, while carriers injected in aBP will not contribute to the signal. However, as shown by the blue solid squares in Figure 2(a), we observed a signal that is a few times smaller and decays at a slower rate. To better compare this signal with that from the ML WS_2 region, it was multiplied by 3.9, as shown by the blue open squares. Clearly, the majority of the signal decays slower than ML WS_2. The significant differences in both the magnitude and the dynamics of the two signals strongly suggest that there is substantial interlayer transfer from WS_2 to aBP.

Close examination of the signal from the heterostructure revealed that the scaled signal can be fit by a tri-exponential function, $\Delta R/R_0(t) = A_1\exp(-t/\tau_1)+A_2\exp(-t/\tau_2)+A_3\exp(-t/\tau_3)$ (black curve), with parameters of A_1, A_2, and A_3 of $2.4, 1.0$, and 0.6×10^{-3}, and τ_1, τ_2, and τ_3 of $0.7\pm0.1, 19.6\pm2$, and 697 ± 150 ps. The sub-ps component contributes to about 60 % of the total signal, which is similar to the ML WS_2 data. It can be attributed to the same origin of exciton formation. the other two time constants show that the carrier lifetime in WS_2 is significantly extended in the heterostructure. Power-dependence measurement also confirms that dynamics is independent of the injected carrier density and the signal magnitude is proportional to the density (see ESI, Figure S2).

The possible candidates for interlayer transfer include energy transfer and charge transfer. The energy transfer can be achieved by either Fröster mechanism [54], where elimination of one exciton in WS_2 induces an exciton or electron-hole pair in aBP, or Dexter mechanism [55,56], where an exciton moves from WS_2 to aBP. In both cases, however, the decay of the signal should be faster than ML WS_2 since the energy transfer provides an additional channel for reducing the carrier density in WS_2. This contradicts to the data. On the other hand, charge transfer (either electrons or holes) from WS_2 to aBP would leave one type of carriers in WS_2, causing a smaller but long-living signal since their recombination will be suppressed by charge separation. Both these features are consistent with the data. Given the large valence band offset between WS_2 and crystalline BP [Figure 1(b)], we expect the transferred carriers to be the holes.

Based on this interpretation and the pronounced PL quenching shown in Figure 1(c), the hole transfer from WS_2 to aBP occurs on a time scale much shorter than the exciton lifetime in ML WS_2. The reduced differential reflection signal of the heterostructure in comparison to WS_2 suggests that the transfer occurs on a time scale comparable to or much shorter than the pulse width of about 0.3 ps. Otherwise, the initial peak of the signal should be similar between the two regions, and there would be an additional decay component that is shorter than 13 ps. Once the holes transferred, the electrons in WS_2 are separated from holes, and thus have an extended lifetime of about 700 ps. The extended carrier lifetime due to charge separation is consistent with previous observations in various type-II van der Waals het-

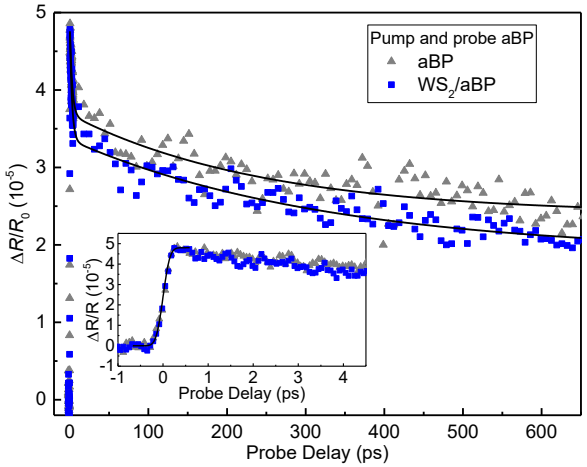

Fig. 3 Time-resolved differential reflection measurements with a 1.55-eV pump and a 0.8-eV probe. Solid symbols represent results from different regions of the same sample. Open symbols is scaled for better comparison. The inset provides a closer look of the data near zero probe delay.

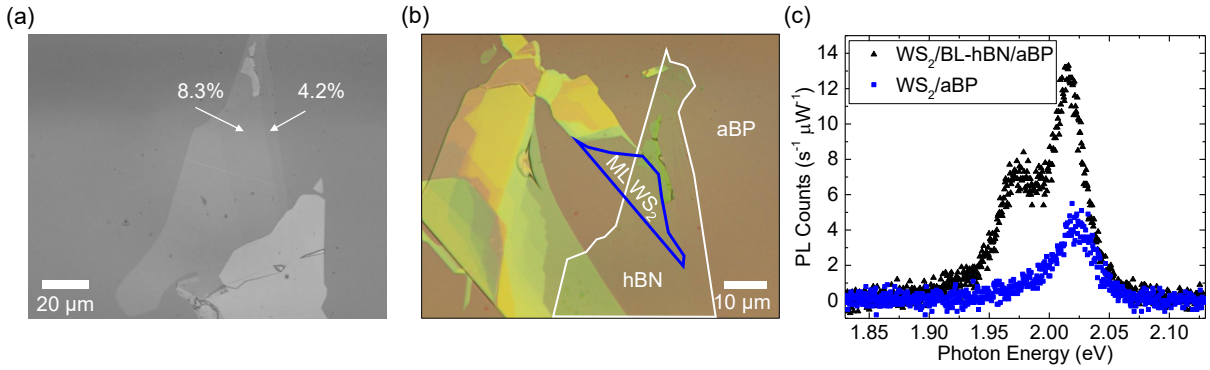

Fig. 4 (a) The green-channel image of the hBN flake on aBP before the WS_2 flake was transferred. The regions with contrasts of 4.2% and 8.3% are identified as monolayer and bilayer, respectively. (b) Optical microscope images of the sample after a WS_2 monolayer was transferred partially on aBP and partially on the bilayer region of hBN. (c) Photoluminescence spectra of ML WS_2 directly on aBP (blue symbols) and on bilayer hBN (black).

erostructures[17,18,57–59]. Finally, we attribute the τ_2 process to the recombination of excitons in WS_2, with holes that do not transfer. It was known that interfacial contaminations[60] can separate the two layers and block interlayer transfer. In the measurement, the region of the sample excited by the laser spots inevitably contains parts with a relatively poor interface. Excitons in these regions recombine efficiently due to the lack of charge transfer, producing this WS_2-like process.

3.3 Lack of Electron Transfer from aBP to WS_2

The lack of electron transfer from WS_2 to aBP appears to suggest that the CBM of WS_2 is lower than aBP, as plotted in Figure 1(b). Therefore, it is interesting to study whether electrons in aBP can transfer to WS_2, which is allowed by the band alignment. In the measurement summarized in Figure 2, the aBP layer was also excited. However, since the probe senses carriers in WS_2 and cannot distinguish between electrons and holes, it is difficult to isolate potential contributions from the electrons transferred from aBP.

To better study the potential transfer of electrons from aBP to WS_2, we performed another set of measurements where only aBP is pumped and probed. Here, a 1.55-eV pump was used to inject carriers in aBP, which are probed by a 0.8-eV pulse that is tuned to its bandgap. We first studied the aBP sample. The differential reflection with a pump fluence of about 50 μJ cm^{-2} is on the order of 5×10^{-5}, as shown by the gray triangles in Figure 3. This is reasonably consistent with our recent measurements on similar samples[53]. As shown in the inset, the signal raises to a peak quickly. The solid line in the inset is the integral of a Gaussian function with a FWHM of about 0.3 ps. The decay of the signal was fit by an bi-exponential function with a background, $\Delta R/R_0(t) = A_0 + A_1\exp(-t/\tau_1) + A_2\exp(-t/\tau_2)$, with the parameters of A_0, A_1, A_2 of $2.4, 1.6, 1.3\times10^{-5}$, and τ_1, τ_2 of 2.9 ± 0.6 and 244 ± 50 ps, respectively. We can attribute the τ_1 process to thermalization or exciton formation, and τ_2 to photocarrier lifetime in aBP. The background is likely induced by trapping of carriers by defects or thermal effects. The most important finding in this set of measurements is that, the signal obtained from the WS_2/aBP heterostructure region is very similar to aBP, as shown by the blue squares in Figure 3. By fitting the data with the same function, we found that for the heterostructure, A_0, A_1, and A_2 are $1.9, 1.5$, and 1.5×10^{-5}, with τ_1 and τ_2 of 2.7 ± 0.6 and 226 ± 50 ps.

The observation that WS_2 does not introduce noticeable changes on the carrier dynamics in aBP is solid evidence that electrons excited in aBP cannot transfer to WS_2 during their lifetime in aBP: If electrons could transfer from aBP to WS_2, such an additional channel would cause a change of the signal. That is, the signal would have a fast-decay component, due to loss of electrons to WS_2, followed by a very slow component due to extended lifetime of holes that are separated from the electrons. Since the signals from the two samples are very similar, we can conclude that electron transfer does not occur in the time scale studied.

The lack of electron transfer from aBP to WS_2 indicates that although efficient charge transfer can occur from the crystalline to amorphous layers, the opposite transfer is inefficient. This can be attributed to the amorphous nature of aBP: Due to the lack of a long-range lattice, electron states in aBP are expected to be largely localized. The localization of the electron wavefunction can prohibit transfer to WS_2 even if there are lower energy states available in WS_2. It is also possible that aBP does not have a well-defined bandedge, and hence there exist conduction band states below WS_2.

3.4 Control of Charge Transfer and Trion Formation

Having demonstrated the ultrafast hole transfer from WS_2 to aBP and the lack of electron transfer from aBP to WS_2, we next explored control of charge transfer by using a thin hBN barrier. We first exfoliated a thin hBN flake onto PDMS and then transferred it to on top of aBP. Figure 4(a) shows the green-channel microscope image of this flake, which clearly shows step-like contrasts with regions of 4.2% and 8.3%, as indicated in the figure. Previously, it has been shown that these contrasts correspond to monolayer phosphorene and bilayer BP flakes[61,62]. We next transferred a WS_2 ML flake partially on the bilayer hBN regions. The black triangles in Figure 4(c) show the PL spectrum from part of the WS_2 flake on bilayer hBN under the 405-nm excitation. The main peak

is slightly shifted to to the low energy side compared to WS_2/aBP (blue squares). Its peak is about 3 times higher than WS_2/aBP, and is thus about 8 times lower than WS_2 ML [Figure 4(c)]. This feature shows that the bilayer hBN can slow down the hole transfer from WS_2 to aBP despite of its ultrasmall thickness. However, the quenching factor of 8 compared to WS_2 ML shows that the hole transfer is still rather efficient. It is interesting to note that a new peak on the low-energy side of the main WS_2 peak was observed in WS_2/bilayer-hBN/aBP, which origin is subject to further investigations.

4 Conclusions

In summary, we have shown that ultrafast and efficient charge transfer can occur from a monolayer crystal to an amorphous semiconducting ultrathin film. We have fabricated heterostructures of monolayer WS_2 and 2-nm amorphous black phosphorus. Significant photoluminescence quenching of WS_2 induced by the amorphous black phosphorus layer indicates effecient excitation transfer from WS_2 to amorphous black phosphorus. The photocarrier dynamics in the heterostructure as well as the individual component layers of WS_2 and amorphous black phosphorus were studied by transient absorption measurements in reflection geometry. By selectively pumping and probing each layer, we found evidence that holes injected in WS_2 transfer to amorphous black phosphorus on an ultrashort time scale on the order of 100 fs or shorter. On the other hand, electrons in neither WS_2 nor amorphous black phosphorus can transfer to the other layer. We attribute the lack of electron transfer from amorphous black phosphorus to WS_2 to the localized nature of electronic states in amorphous materials. Furthermore, we show that a bilayer hBN can effectively change the hole transfer process. These results introduce amorphous black phosphorus as a building block for van der Waals heterostructures, reveal new information for understanding interlayer charge transfer, and provide a method to electrically connect to amorphous materials by van der Waals interfaces.

5 Acknowledgement

This work was supported by the National Science Foundation of USA (DMR-1505852) and the Research Grants Council of Hong Kong (Projects: PolyU 153271/16P and 153039/17P).

References

1 E. Gibney, *Nature*, 2015, **522**, 274–276.

2 A. H. C. Neto and K. Novoselov, *Rep. Prog. Phys.*, 2011, **74**, 082501.

3 Q. H. Wang, K. Kalantar-Zadeh, A. Kis, J. N. Coleman and M. S. Strano, *Nat. Nanotechnol.*, 2012, **7**, 699–712.

4 S. Z. Butler, S. M. Hollen, L. Cao, Y. Cui, J. A. Gupta, H. R. Gutiérrez, T. F. Heinz, S. S. Hong, J. Huang, A. F. Ismach, E. Johnston-Halperin, M. Kuno, V. V. Plashnitsa, R. D. Robinson, R. S. Ruoff, S. Salahuddin, J. Shan, L. Shi, M. G. Spencer, M. Terrones, W. Windl and J. E. Goldberger, *ACS Nano*, 2013, **7**, 2898.

5 Z. Lin, A. McCreary, N. Briggs, S. Subramanian, K. H. Zhang, Y. F. Sun, X. F. Li, N. J. Borys, H. T. Yuan, S. K. Fullerton-Shirey, A. Chernikov, H. Zhao, S. McDonnell, A. M. Lindenberg, K. Xiao, B. J. LeRoy, M. Drndic, J. C. M. Hwang, J. Park, M. Chhowalla, R. E. Schaak, A. Javey, M. C. Hersam, J. Robinson and M. Terrones, *2D Mater.*, 2016, **3**, 042001.

6 A. K. Geim and I. V. Grigorieva, *Nature*, 2013, **499**, 419–425.

7 Y. Liu, N. O. Weiss, X. Duan, H.-C. Cheng, Y. Huang and X. Duan, *Nat. Rev. Mater.*, 2016, **1**, 16042.

8 K. S. Novoselov, A. Mishchenko, A. Carvalho and A. H. C. Neto, *Science*, 2016, **353**, 461.

9 W. J. Yu, Y. Liu, H. Zhou, A. Yin, Z. Li, Y. Huang and X. Duan, *Nat. Nanotechnol.*, 2013, **8**, 952–958.

10 D. D. Fazio, I. Goykhman, D. Yoon, M. Bruna, A. Eiden, S. Milana, U. Sassi, M. Barbone, D. Dumcenco, K. Marinov, A. Kis and A. C. Ferrari, *ACS Nano*, 2016, **10**, 8252–8262.

11 W. J. Yu, Q. A. Vu, H. Oh, H. G. Nam, H. L. Zhou, S. Cha, J. Y. Kim, A. Carvalho, M. Jeong, H. Choi, A. H. C. Neto, Y. H. Lee and X. F. Duan, *Nat. Commun.*, 2016, **7**, 13278.

12 L. Britnell, R. M. Ribeiro, A. Eckmann, R. Jalil, B. D. Belle, A. Mishchenko, Y.-J. Kim, R. V. Gorbachev, T. Georgiou, S. V. Morozov, A. N. Grigorenko, A. K. Geim, C. Casiraghi, A. H. C. Neto and K. S. Novoselov, *Science*, 2013, **340**, 1311–1314.

13 S. V. Morozov, K. S. Novoselov, M. I. Katsnelson, F. Schedin, D. C. Elias, J. A. Jaszczak and A. K. Geim, *Phys. Rev. Lett.*, 2008, **100**, 016602.

14 H.-L. Liu, C.-C. Shen, S.-H. Su, C.-L. Hsu, M.-Y. Li and L.-J. Li, *Appl. Phys. Lett.*, 2014, **105**, 201905.

15 M. H. Chiu, C. D. Zhang, H. W. Shiu, C. P. Chuu, C. H. Chen, C. Y. S. Chang, C. H. Chen, M. Y. Chou, C. K. Shih and L. J. Li, *Nat.Commun.*, 2015, **6**, 7666.

16 H. Fang, C. Battaglia, C. Carraro, S. Nemsak, B. Ozdol, J. S. Kang, H. A. Bechtel, S. B. Desai, F. Kronast, A. A. Unal, G. Conti, C. Conlon, G. K. Palsson, M. C. Martin, A. M. Minor, C. S. Fadley, E. Yablonovitch, R. Maboudian and A. Javey, *Proc. Natl. Acad. Sci. U. S. A.*, 2014, **111**, 6198–6202.

17 X. Hong, J. Kim, S. F. Shi, Y. Zhang, C. Jin, Y. Sun, S. Tongay, J. Wu, Y. Zhang and F. Wang, *Nat. Nanotechnol.*, 2014, **9**, 682–686.

18 F. Ceballos, M. Z. Bellus, H. Y. Chiu and H. Zhao, *ACS Nano*, 2014, **8**, 12717–12724.

19 P. Rivera, J. R. Schaibley, A. M. Jones, J. S. Ross, S. Wu, G. Aivazian, P. Klement, K. Seyler, G. Clark, N. J. Ghimire, J. Yan, D. G. Mandrus, W. Yao and X. Xu, *Nat. Commun.*, 2015, **6**, 6242.

20 C. H. Lee, G. H. Lee, A. M. van der Zande, W. Chen, Y. Li, M. Han, X. Cui, G. Arefe, C. Nuckolls, T. F. Heinz, J. Guo, J. Hone and P. Kim, *Nat. Nanotechnol.*, 2014, **9**, 676–681.

21 P. Rivera, K. L. Seyler, H. Y. Yu, J. R. Schaibley, J. Q. Yan, D. G. Mandrus, W. Yao and X. D. Xu, *Science*, 2016, **351**, 688–691.

22 J. R. Schaibley, P. Rivera, H. Y. Yu, K. L. Seyler, J. Q. Yan, D. G. Mandrus, T. Taniguchi, K. Watanabe, W. Yao and X. D. Xu, *Nat. Commun.*, **7**, 13747.

23 W. G. Xu, W. W. Liu, J. F. Schmidt, W. J. Zhao, X. Lu, T. Raab, C. Diederichs, W. B. Gao, D. V. Seletskiy and Q. H. Xiong, *Nature*, 2017, **541**, 62.

24 A. T. Hanbicki, H.-J. Chuang, M. R. Rosenberger, C. S. Hell-

berg, S. V. Sivaram, K. M. McCreary, I. I. Mazin and B. T. Jonker, *ACS Nano*, 2018, **12**, 4719–4726.
25 Y. Wang, Z. Wang, W. Yao, G. B. Liu and H. Y. Yu, *Phys. Rev. B*, 2017, **95**, 115429.
26 J. Sun, H. W. Lee, M. Pasta, H. T. Yuan, G. Y. Zheng, Y. M. Sun, Y. Z. Li and Y. Cui, *Nat. Nanotechnol.*, 2015, **10**, 980.
27 M. Q. Huang, S. M. Li, Z. F. Zhang, X. Xiong, X. F. Li and Y. Q. Wu, *Nat. Nanotechnol.*, 2017, **12**, 1148.
28 J. Shim, S. Oh, D. H. Kang, S. H. Jo, M. H. Ali, W. Y. Choi, K. Heo, J. Jeon, S. Lee, M. Kim, Y. J. Song and J. H. Park, *Nat. Commun.*, 2016, **7**, 13413.
29 D.-H. Kwak, H.-S. Ra, M.-H. Jeong, A.-Y. Lee and J.-S. Lee, *Adv. Mater. Interfaces*, 2018, **5**, 1800671.
30 F. Wang, Z. X. Wang, K. Xu, F. M. Wang, Q. S. Wang, Y. Huang, L. Yin and J. He, *Nano Lett.*, 2015, **15**, 7558–7566.
31 A. Vargas, F. Z. Liu, C. Lane, D. Rubin, I. Bilgin, Z. Hennighausen, M. DeCapua, A. Bansil and S. Kar, *Sci. Adv.*, 2017, **3**, e1601741.
32 D. Zhong, K. L. Seyler, X. Y. Linpeng, R. Cheng, N. Sivadas, B. Huang, E. Schmidgall, T. Taniguchi, K. Watanabe, M. A. McGuire, W. Yao, D. Xiao, K. M. C. Fu and X. D. Xu, *Sci. Adv.*, 2017, **3**, e1603113.
33 L. Niu, X. F. Liu, C. X. Cong, C. Y. Wu, D. Wu, T. R. Chang, H. Wang, Q. S. Zeng, J. D. Zhou, X. L. Wang, W. Fu, P. Yu, Q. D. Fu, S. Najmaei, Z. H. Zhang, B. I. Yakobson, B. K. Tay, W. Zhou, H. T. Jeng, H. Lin, T. C. Sum, C. Jin, H. Y. He, T. Yu and Z. Liu, *Adv. Mater.*, 2015, **27**, 7800–7808.
34 H. C. Cheng, G. M. Wang, D. H. Li, Q. Y. He, A. X. Yin, Y. Liu, H. Wu, M. N. Ding, Y. Huang and X. F. Duan, *Nano Lett.*, 2016, **16**, 367–373.
35 X. Liu, J. Gu, K. Ding, D. J. Fan, X. E. Hu, Y. W. Tseng, Y. H. Lee, V. Menon and S. R. Forrest, *Nano Lett.*, 2017, **17**, 3176–3181.
36 Y. Huang, F. W. Zhuge, J. X. Hou, L. Lv, P. Luo, N. Zhou, L. Gan and T. Y. Zhai, *ACS Nano*, 2018, **12**, 4062–4073.
37 T. Kafle, B. Kattel, S. D. Lane, T. Wang, H. Zhao and W. L. Chan, *ACS Nano*, 2017, **11**, 10184–10192.
38 A. Shah, P. Torres, R. Tscharner, N. Wyrsch and H. Keppner, *Science*, 1999, **285**, 692–698.
39 P. G. Lecomber, W. E. Spear and A. Ghaith, *Electron. Lett.*, 1979, **15**, 179–181.
40 K. Nomura, H. Ohta, A. Takagi, T. Kamiya, M. Hirano and H. Hosono, *Nature*, 2004, **432**, 488–492.
41 K. S. Suslick, S. B. Choe, A. A. Cichowlas and M. W. Grinstaff, *Nature*, 1991, **353**, 414–416.
42 R. D. L. Smith, M. S. Prevot, R. D. Fagan, Z. P. Zhang, P. A. Sedach, M. K. J. Siu, S. Trudel and C. P. Berlinguette, *Science*, 2013, **340**, 60–63.
43 Z. Yang, J. Hao, S. Yuan, S. Lin, H. M. Yau, J. Dai and S. P. Lau, *Adv. Mater.*, 2015, **27**, 3748–3754.
44 Y. Z. Guo and J. Robertson, *Appl. Phys. Lett.*, 2016, **108**, 233104.
45 Y. Cai, G. Zhang and Y. W. Zhang, *Sci. Rep.*, 2014, **4**, 6677.
46 Z. Ye, T. Cao, K. O'Brien, H. Zhu, X. Yin, Y. Wang, S. G. Louie and X. Zhang, *Nature*, 2014, **513**, 214–218.
47 B. Zhu, H. Zeng, J. Dai, Z. Gong and X. Cui, *Proc. Nat. Acad. Sci. USA*, 2014, **111**, 11606–11611.
48 W. J. Zhao, Z. Ghorannevis, L. Q. Chu, M. L. Toh, C. Kloc, P. H. Tan and G. Eda, *ACS Nano*, 2013, **7**, 791–797.
49 N. Peimyoo, J. Z. Shang, C. X. Cong, X. N. Shen, X. Y. Wu, E. K. L. Yeow and T. Yu, *ACS Nano*, 2013, **7**, 10985–10994.
50 F. Ceballos, Q. Cui, M. Z. Bellus and H. Zhao, *Nanoscale*, 2016, **8**, 11681–11688.
51 C. Mai, Y. G. Semenov, A. Barrette, Y. F. Yu, Z. H. Jin, L. Y. Cao, K. W. Kim and K. Gundogdu, *Phys. Rev. B*, 2014, **90**, 041414.
52 J. He, D. He, Y. Wang, Q. Cui, F. Ceballos and H. Zhao, *Nanoscale*, 2015, **7**, 9526.
53 M. Z. Bellus, Z. B. Yang, J. H. Hao, S. P. Lau and H. Zhao, *2D Mater.*, 2017, **4**, 025063.
54 F. J. M. Hoeben, P. Jonkheijm, E. W. Meijer and A. Schenning, *Chem. Rev.*, 2005, **105**, 1491–1546.
55 D. L. Dexter, *J. Chem. Phys.*, 1953, **21**, 836–850.
56 C. B. Murphy, Y. Zhang, T. Troxler, V. Ferry, J. J. Martin and W. E. Jones, *J. Phys. Chem. B*, 2004, **108**, 1537–1543.
57 F. Ceballos, M. Z. Bellus, H. Y. Chiu and H. Zhao, *Nanoscale*, 2015, **7**, 17523–17528.
58 B. Peng, G. Yu, X. Liu, B. Liu, X. Liang, L. Bi, L. Deng, T. C. Sum and K. P. Loh, *2D Mater.*, 2016, **3**, 025020.
59 H. M. Zhu, J. Wang, Z. Z. Gong, Y. D. Kim, J. Hone and X. Y. Zhu, *Nano Lett.*, 2017, **17**, 3591–3598.
60 S. J. Haigh, A. Gholinia, R. Jalil, S. Romani, L. Britnell, D. C. Elias, K. S. Novoselov, L. A. Ponomarenko, A. K. Geim and R. Gorbachev, *Nat. Mater.*, 2012, **11**, 764–767.
61 D. Golla, K. Chattrakun, K. Watanabe, T. Taniguchi, B. J. LeRoy and A. Sandhu, *Appl. Phys. Lett.*, 2013, **102**, 161906.
62 R. Gorbachev, I. Riaz, R. Nair, R. Jalil, L. Britnell, B. Belle, E. Hill, K. Novoselov, K. Watanabe, T. Taniguchi, A. Geim and P. Blake, *Small*, **7**, 465–468.